Dynamic-Absorption Spectral Contours: Vibrational Phase-Dependent Resolution of Low-Frequency Coherent Wave-Packet Motion of IR144 on the Ground-State and Excited-State $\pi \rightarrow \pi^*$ Surfaces

Elizabeth A. Carson,[†] William M. Diffey,[†,‡] Katherine R. Shelly, Sanela Lampa-Pastirk, Kevin L. Dillman, James M. Schleicher,[§] and Warren F. Beck*

Department of Chemistry, Michigan State University, 3 Chemistry Building, East Lansing, Michigan 48824

Received: May 1, 2003; In Final Form: December 18, 2003

We have characterized the femtosecond dynamic-absorption spectrum from the tricarbocyanine dye IR144 with the aid of a new approach that uses time-probe-wavelength contour lines to project the phase relationships between the coherent wave-packet motions on the ground-state and excited-state potential-energy surfaces. The distinct phase of the waveform carried by a dynamic-absorption contour line reports the motion of a single wave packet. The spectrum from IR144 exhibits *four* regions of alternating contour phase; simulations show that this interference pattern results from the antiphase motion and partial spectral overlap of the ground-state depletion and stimulated-emission spectra and the narrowing of the spectra that occurs when the excited-state and ground-state wave packets reach their turning points. The Fourier-magnitude spectra of contour lines and intensity transients observed in the spectral region, which are assigned to the turning point of the ground-state wave packet, have been compared to those obtained in the long-wavelength-limit spectral region that is associated with the excited-state wave packet. The intensities and frequencies of eleven modes observed over the 15−634 cm^{-1} region suggest that the excited-state wave packet rapidly moves from the Franck−Condon geometry to a region of the potential-energy surface that is relatively flat with respect to the global normal coordinates that bend and twist the conjugated polyene backbone of IR144. These coordinates are evidently anharmonically coupled to high-frequency modes that are not impulsively excited by the 12-fs pulses used in the dynamic-absorption experiments.

1. Introduction

More than 10 years ago, Shank, Mathies, and co-workers[1−9] showed that the resonant impulsive excitation of large electronic chromophores in condensed phases and in proteins results in a nonstationary absorption/stimulated-emission spectrum. When monitored with a short, delayed probe pulse that is resonant with the ground-state absorption spectrum, the intensity of the transmitted probe light is modulated at the normal-mode frequencies that would appear in the resonance Raman spectrum. If the probe pulse is resonant with the stimulated-emission spectrum, the modulation frequencies are those of the excited electronic state. This so-called "dynamic-absorption spectroscopy" was described by Pollard and Mathies[10−13] in terms of the coherent motion of vibronic wave packets (vibrational coherence) on the resonant electronic excited-state and ground-state potential-energy surfaces, the latter produced by stimulated Raman transitions.

A comparison of excited-state and ground-state coherent wave-packet motions permits one to detect excited-state structural rearrangements in terms of mode-specific forces. Ground-state vibrational coherence and conventional resonance Raman intensities identify the normal modes that contribute to wave-packet motion in the neighborhood of the Franck−Condon excited-state structure, which overlaps vertically with the equilibrium ground-state structure. In the simplest situation, the active modes are those with coordinates that are displaced with respect to the equilibrium ground-state structure, so the excited-state potential-energy surface is sloped at the Franck−Condon structure.[14] If the excited-state vibrational coherence is different from that observed on the ground state, the molecule evolves on the excited-state potential energy surface to a structure where the forces are different from those in the Franck−Condon region.

Unfortunately, for large molecules with small Stokes shifts, a clear distinction between the ground-state and excited-state vibrational coherence cannot be made solely on the basis of probe wavelength because the ground-state depletion and stimulated-emission signals overlap near the 0−0 vibronic transition. A more powerful approach uses the distinct *phase* of the vibrations on the two surfaces. Because of the back-and-forth motion by a wave packet on a particular surface, the pump−probe signal exhibits a sweep of the modulation time maxima with respect to the probe wavelength between two limits that correspond to a π phase shift.[9,15−20] Therefore, one might expect to be able to define the spectral regions that correspond to the motions of the excited-state and ground-state wave packets on the basis of their expected π shifts of phase. In practice, a mode-specific analysis of the phase in pump−probe transients is very difficult where spectral overlaps occur.[21] In this contribution, we show how a *contour* representation of the dynamic-absorption intensity-wavelength-delay surface permits one to obtain the phase information *by inspection*. The contour lines exhibit an easily interpreted interference pattern

* Author to whom correspondence should be addressed. E-mail: beckw@msu.edu.

[†] These authors made equal contributions to the paper.

[‡] Current address: Weapons Sciences Directorate, U. S. Army Aviation and Missile Command, Redstone Arsenal, AL35898.

[§] Current address: Department of Chemistry, Yale University, 225 Prospect St., New Haven, CT 06520-8107.

10.1021/jp035176c CCC: $27.50
Published on Web 02/04/2004

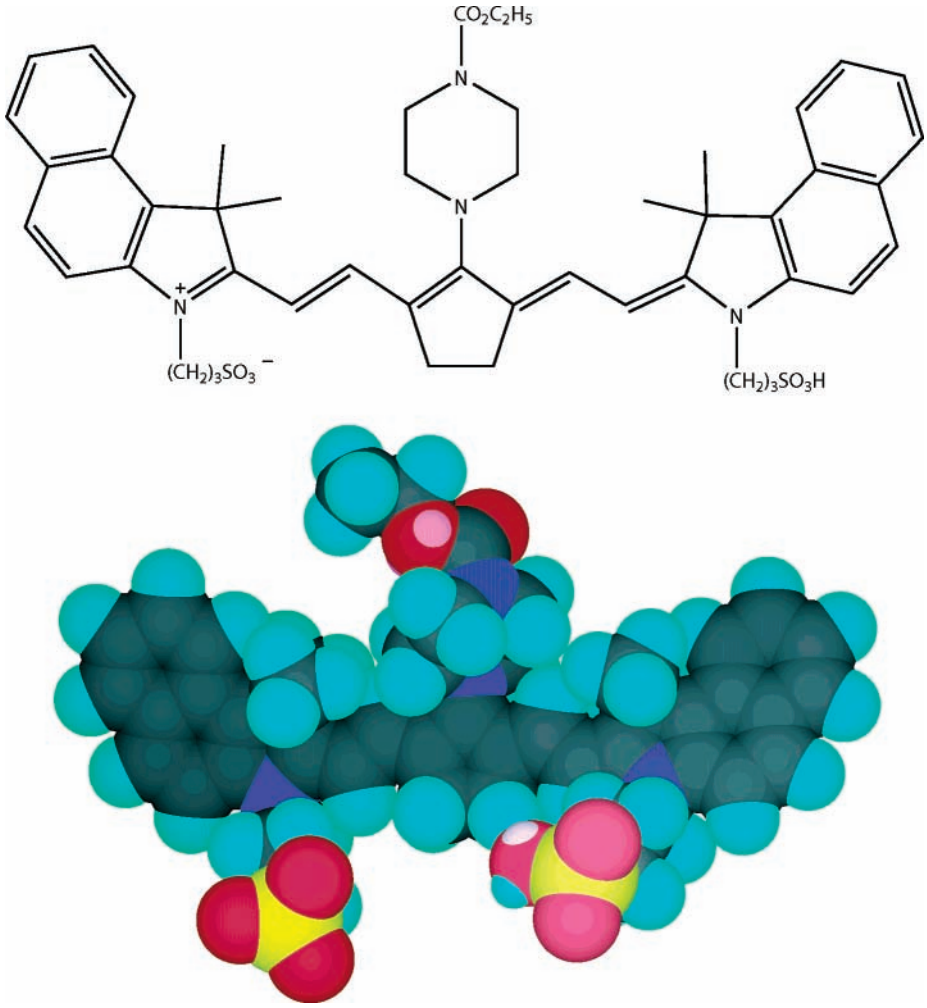

Figure 1. Structure of the all-trans configuration of IR144; the space-filling (CPK) representation is that of the energy-minimized structure obtained with the MM2 force field.

that results where the excited-state and ground-state signals overlap.

We have made a first application of dynamic-absorption contours in the characterization of ground-state and excited-state vibrational coherence in the tricarbocyanine dye IR144 (anhydro-11-(4-ethoxycarbonyl-1-piperazinyl)-10,12-ethylene-3,3,3′,3′-tetramethyl-1,1′-di-(3-sulfopropyl)-4,5,4′,5′-dibenzoindotricarbocyanine hydroxide; see Figure 1), which is perhaps the most important member of a set of tricarbocyanine dyes that have been used in the development of nonlinear spectroscopic methods that probe ultrafast solvent dynamics in liquids[22−26] and on surfaces.[27] In all this work, it is assumed that the structure of IR144 is invariant during the early solvent reorganization dynamics. This assumption is encouraged by a distinctive feature of the structure of IR144—the central five-membered ring—which might be expected to inhibit trans-cis isomerization of the conjugated polyene. However, the results discussed in this paper suggest that the structure of IR144 evolves significantly during the first few vibrations following excitation. Based on ground-state electronic-structure and normal-mode calculations, we assign a strong 10−15 cm^{-1} feature to global modes that involve torsion and deformation of the conjugated polyene. Excited-state wave-packet motion along these coordinates carry IR144 from its planar ground-state structure to a structure that is bent or twisted along the polyene backbone.

2. Experimental Section

Sample Preparation. IR144 was obtained from Exciton and used as received. Samples for femtosecond spectroscopy were dissolved in methanol (spectrophotometric grade, Spectrum) to obtain an absorbance of 0.4−0.6 at 800 nm for a 1-mm path length; the IR144 solution was passed through a 0.22-μm filter prior to use.

Continuous-Wave Spectroscopy. Fluorescence spectra were obtained at room temperature (23 °C) with a home-built visible/near-infrared spectrofluorimeter built around a liquid-nitrogen-cooled charge-coupled device (CCD) detector. Excitation light from a quartz-halogen lamp (Jobin-Yvon, model AH10) was selected by a monochromator (Spex, model 1681) that was operated with a spectral bandpass of 4 nm. On its path to the sample position, the excitation beam passed through a fused-silica optical fiber bundle, a Glan−Thompson calcite polarizer, and a fused-silica focusing lens with a focal length of 5 cm. The horizontal line of fluorescence emitted by the sample was collected at an angle of 90° from the direction of the excitation beam by a fused-silica lens with a focal length of 5 cm. To obtain dichroism-free spectra, a Glan−Thompson calcite polarizer analyzed the fluorescence beam at the magic angle, 54.7°, with respect to the plane of the excitation-beam polarizer. The transmitted fluorescence image was rotated to the vertical by a pair of silver mirrors and then focused onto the entrance slit of a spectrograph (Spex, model 270m) by a fused-silica lens with a focal length of 5 cm. The spectrograph was equipped with a

600-grooves/mm ruled diffraction grating, which exposed the CCD detector to a 370-nm-wide region of the emission spectrum. The 0.5-mm entrance slit set the effective bandpass of the spectrograph to 3.33 nm. The CCD system, which consisted of a Spex SpectrumOne CCD detector and a model CCD2000 controller, used an EEV 800 × 2048-pixel, back-illuminated spectroscopic CCD chip; Spex SpectraMax software was used for data acquisition.

Scattered light was removed from the fluorescence spectra through subtraction of a blank solvent-only spectrum that was recorded under the same measurement conditions with the same cuvette. The spectra were then corrected for the sensitivity of the spectrofluorimeter with respect to wavelength; a quartz-halogen lamp of known irradiance with respect to emission wavelength (Ocean Optics) was used at the sample position to obtain the correction curve for the spectral response. The diffraction grating (optimized for first-order diffraction at 500 nm) and the silicon CCD (peak sensitivity in the 800-nm region) results in a rapidly decreasing signal/noise ratio in the 1000-nm region; the signal could not be used at wavelengths of >1050 nm. When plotted as a function of wavenumber, the fluorescence intensity was multiplied by the square of the wavelength, λ^2, as required to compensate for the fixed effective spectral bandpass of the emission spectrometer.[28]

Absorption spectra were obtained with a 2-nm spectral bandpass at room temperature (22 °C), using a Hitachi model U-2000 spectrometer and LabVIEW (National Instruments) routines.

Femtosecond Spectroscopy. Dynamic-absorption spectroscopy was performed with two femtosecond pump−probe spectrometers that were built around self-mode-locked titanium−sapphire oscillators. The main features of the apparatus have been discussed previously,[29,30] but certain important changes are discussed here. For short-pulse, broad-spectrum experiments, a home-built titanium−sapphire oscillator based on the Murnane−Kapteyn[31,32] design was used as the light source; long-pulse, narrow-spectrum experiments used a Mira9000 oscillator (Coherent) that was equipped with X-wave broad-tuning-range cavity optics. Both oscillators were continuously pumped by Verdi (Coherent) 5-W lasers and were used at the natural pulse-repetition rate (76 MHz) without pulse selection. Extracavity pulse compression used LaKL21 and SF10 prism pairs, respectively.

Both spectrometers used rapid-scanning[33] modified Mach−Zehnder interferometers[29] of an improved design. A galvanometer-driven translation stage and retroreflector (Clark-MXR ODL-150) scanned the pump-pulse time-of-flight delay. The pump beam was amplitude-modulated at 100 kHz by a $\lambda/2$ retarding photoelastic modulator (Hinds Instruments) and a Glan-laser calcite polarizer (Karl Lambrecht). The plane of polarization of the probe beam was analyzed at an angle of 45° with respect to the plane of polarization of the pump beam by a Glan-laser calcite polarizer; a mica zero-order $\lambda/2$ plate (Karl Lambrecht) prior to the polarizer was rotated to control the probe intensity. A BK7 lens with a focal length of 10 cm was used to focus the pump (125 pJ/pulse) and probe beam (30 pJ/pulse) onto the position of the sample. After transmitting the sample and after recollimation, the probe beam was analyzed at an angle of 63.44° with respect to the pump polarization by another Glan-laser calcite polarizer to obtain dichroism-free signals.[34] The transmitted probe beam was then passed through a monochromator (Spex 270m or Acton Research SpectraPro150, with spectral bandpasses of 4 and 2 nm, respectively) and detected by a amplified silicon photodiode (Thorlabs model PDA520).

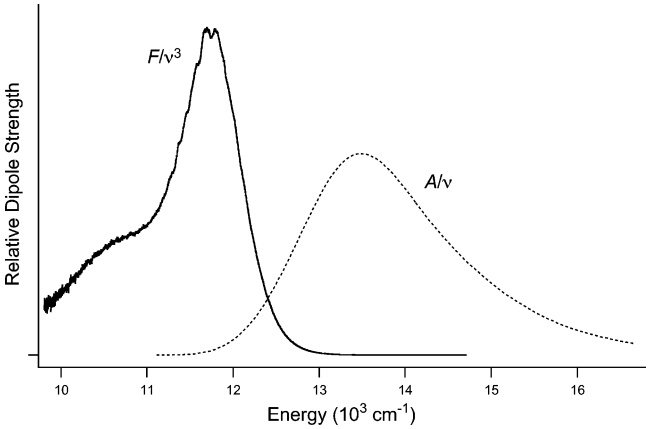

Figure 2. Continuous-wave absorption and fluorescence spectra from IR144 in methanol, plotted as relative dipole strengths A/ν and F/ν^3, respectively. Spectra are normalized to unit area. The fluorescence spectrum was excited at 790 nm (12 600 cm^{-1}).

The photodiode signal was demodulated by a digital lock-in amplifier (model SRS750 or SRS850, Stanford Research Systems), which was referenced to the 100-kHz pump-amplitude-modulation frequency.

The pump and probe beams were sampled prior to reaching the focusing lens to provide a pair of pulses for autocorrelation analysis during data acquisition. A β-barium borate crystal (Inrad or Cleveland Crystals, 100 μm thick, cut for type I sum-frequency generation with 800-nm input) was placed at the focus of a 10-cm focal-length BK7 lens; the second-harmonic beam was detected by a photomultiplier tube and lock-in amplifier (LIA-MV-200-H, Femto Messtechnik). The group-delay dispersion in the autocorrelation arm of the interferometer was the same as in the sample arm; identical beam splitters, compensator plates, and focusing optics were used.

A sample/hold amplifier and digitizer (National Instruments models SC-2040S/H and PCI-6024E, respectively) recorded the analog outputs of the two lock-in amplifiers (for the pump−probe signal and autocorrelation signal), the transmitted-probe photodiode signal, and the position of the galvanometer (delay reference) signal. The digitization frequency was 17 kHz. The delay axis was repetitively scanned at 1.3 Hz over a 12-ps delay range. During each scan of the delay axis, 7000 data points were acquired, resulting in an effective dwell time per acquired data point of 1.8 fs. The signal-averaging system and monochromator were controlled by LabVIEW routines. We eliminated scan-to-scan delay drift[29] using the autocorrelation signal as a zero-delay-time reference pulse for each scan.

The IR144 sample was held at room temperature (22 °C) in a fused-silica flow cuvette; the path length was 1 mm. The sample flow rate was 6 mL/min. The absorption spectrum of the sample was monitored for changes that resulted from photochemistry or permanent photobleaching.

3. Results

Continuous-Wave Spectroscopy. Figure 2 shows the absorption and fluorescence spectra exhibited by IR144 in methanol solvent at room temperature. The spectra are plotted as $A(\nu)/\nu$ and $F(\nu)/\nu^3$, respectively, with normalization to unit area. The integrals of these quantities report the dipole strength,[28,35] the square of the transition-dipole moment, which is proportional to the Einstein coefficients for absorption and stimulated emission (B_{ab} and B_{ba}, respectively). As plotted, the sum of the spectra can be compared to the time-integrated dynamic-absorption spectrum in the weak-field limit.[12] The

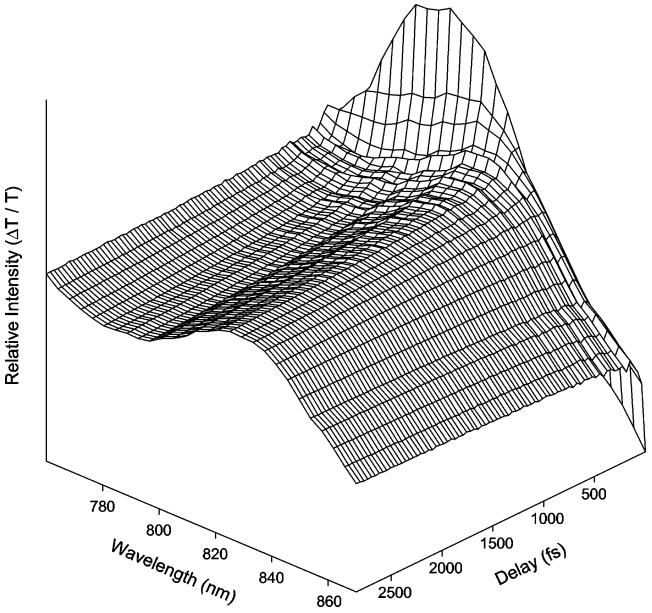

Figure 3. Dynamic-absorption spectrum obtained with 12-fs pulses centered at 790 nm from IR144 in methanol.

fluorescence spectrum exhibits some partially resolved vibronic structure; no structure is observed in the absorption spectrum. The 0−0 vibronic transition occurs in the vicinity of 12 400 cm^{-1} (806 nm), where the two normalized spectra cross.

In the short-pulse (12-fs $sech^2$) dynamic-absorption experiments, the titanium−sapphire laser's spectrum (11 300−13 333 cm^{-1}, with peak intensity at 12 500 cm^{-1}) excites IR144 over a spectral range that starts to the red of the absorption maximum, passes the 0−0 transition, and proceeds onward to cover the red onset. The laser spectrum then spans much of the fluorescence spectrum. Accordingly, as used in the dynamic-absorption experiments as the probe beam, the laser spectrum covers much of the stimulated-emission spectrum and only the red onset of the ground-state depletion spectrum.

Short-Pulse Dynamic-Absorption Experiments. Figure 3 shows a three-dimensional mesh-surface view of a portion of the dynamic-absorption intensity-delay-wavelength surface from IR144 in methanol. A set of single-wavelength pump-induced transmission ($\Delta T/T$) transients was recorded over a 110-nm range of probe wavelengths; the spacing of the probe wavelengths matched the spectral bandpass of the monochromator (4 nm). Initially, the dynamic-absorption spectrum exhibits a hole-burned character, with the overall width far less than anticipated from the sum of the absorption and fluorescence dipole-strength line shapes (see Figure 4, right panel). Within 100 fs, the spectrum splits into two partially resolved peaks, from ground-state depletion and from stimulated emission, and broadens to close to the anticipated width. The stimulated-emission spectrum is red-shifted, compared to the initial position of the hole spectrum; it exhibits a peak near the position of the fluorescence maximum by the 2-ps delay point.

The main panel of Figure 4 shows a contour representation of the dynamic-absorption surface of IR144. The contour plot was obtained from the 4-nm × 1.8-fs data grid, using default settings in the program Igor Pro (Wavemetrics). The program uses bilinear interpolation to obtain a square, high-resolution grid; interpolation along the longer of the two grid axes, the delay axis, was not required. From this grid, contour lines were constructed at 40 discrete intensity levels; the intensity levels were evenly spaced over the full range of intensities in the data set. Similar contour lines were obtained, although with a lower

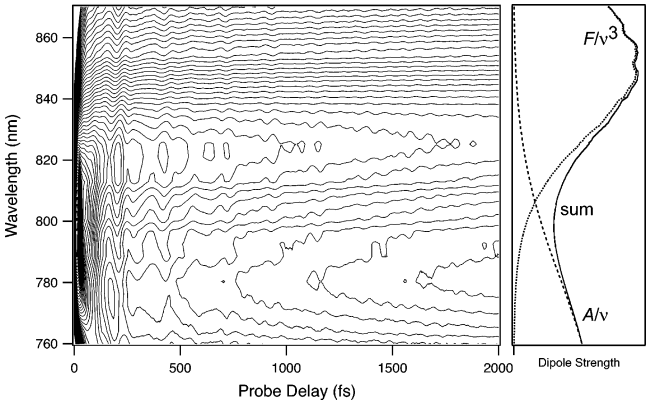

Figure 4. Contour representation of the dynamic-absorption spectrum obtained from IR144 in methanol. Right-hand panel shows the continuous-wave fluorescence-emission spectrum (dotted line), the absorption spectrum (dashed line), and their sum (solid line) plotted as relative dipole strengths on the same wavelength scale.

signal/noise ratio, with data sets recorded with a resolution and spacing of 2 nm.

The contour lines exhibit wavelength oscillations with respect to the delay axis. These oscillations are not as prominent in the mesh-surface representation because of their relatively low amplitude. The wavelength oscillations are clearly grouped into *sets* of contour lines with the *same phase*. Near flat portions of the surface (see Figure 3), the contour lines break off; on slanted portions of the surface, continuous runs of oscillations can be observed, spanning at least the 0−5000 fs delay range.

Four sets of contour lines with alternating phase are observed in Figure 4 as one scans from one wavelength limit to the other. One set runs from the 870-nm red limit of the surface to 830 nm, near the peak of the stimulated-emission spectrum. A second, oppositely phased set ranges from 810 nm to the 780-nm region. The phase inverts again for the set of contour lines that begins at 775 nm and runs to 765 nm. A fourth set is only partially observed at the 760-nm blue limit of the probe spectrum.

Two transients from the data set used to build the dynamic-absorption surface are shown in Figure 5. Intensity oscillations are observed over the 200−5000 fs delay range. The 864-nm transient is chosen from the spectral region covered by the set of contour lines at the red limit of the probe spectrum. The 808-nm transient is chosen from the spectral range covered by the oppositely phased set of contour lines that lies below the first set. The biexponential falling and rising trends that follow the zero-time pump−probe interaction region in the 808- and 864-nm transients, respectively, show the effects of dynamic solvation on the stimulated-emission spectrum (see Figure 3); excited-state population decay occurs on a much longer time scale. In the following, we examine in more detail, the information content carried in the wave-packet oscillations detected in these two spectral regions.

Figure 6 shows an expanded view of the oscillatory portion of two contour lines selected from the set shown in Figure 4. The contour lines were those centered approximately at 808 and 864 nm—the wavelength regions probed by the two transients in Figure 5. The oscillatory portion of each contour line was obtained by subtracting a fitted double-exponential baseline function. The fit started at a delay past the initial fast decay or rise transient (∼150 fs; see Figure 5) and extended to the end of the contour line.

Figure 6 shows that the 808- and 864-nm contour lines exhibit the same oscillatory features but with almost perfectly opposite phases. The arrows in Figure 6 mark extrema in the two traces

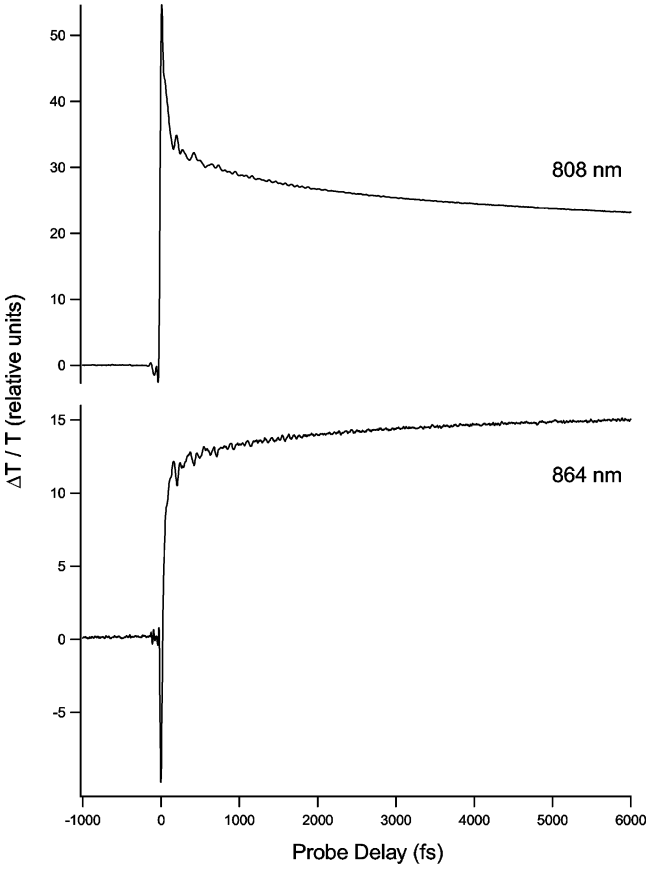

Figure 5. Dynamic-absorption transients obtained from IR144 in methanol, with the transmitted probe light detected at 808 and 864 nm; the maximum signal for the 808-nm transient corresponds to $\Delta T/T = 10^{-4}$.

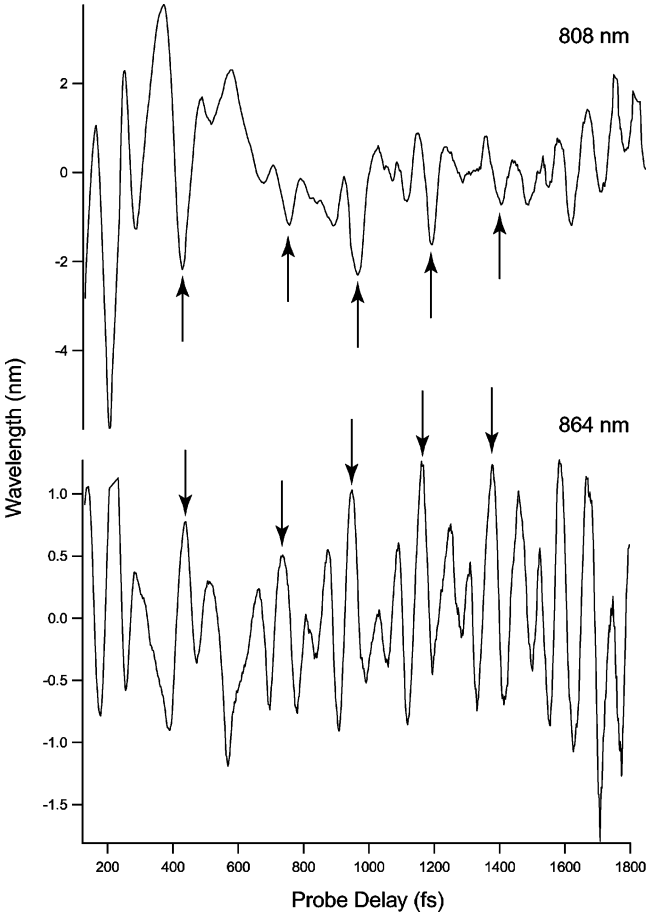

Figure 6. Delay-expanded view of a section of the oscillatory signals obtained from the contour lines centered at 808 and 864 nm in the dynamic-absorption spectrum from IR144 in methanol. These contour lines were selected from the set shown in Figure 4. To illustrate the antiphase character of the two contour lines, arrows mark several extrema at approximately the same delay times.

that occur at almost the same delay point; notice that the antiphased features gradually separate in time, with the 808-nm trace trailing the 864-nm trace. The 808-nm trace also includes an obvious low-frequency oscillation, with a maximum swing at 400 fs and a minimum swing at 1000 fs, which is not as apparent in the 864-nm trace.

Fourier-Magnitude Spectrum Estimation. The next four figures present a Fourier analysis of the oscillatory components observed in transmission-intensity transients and contour lines at the 808- and 864-nm probe wavelengths. The oscillatory portion of each signal was obtained by subtracting a fitted double-exponential baseline function. The oscillatory segment over the 150−4000 fs delay range was multiplied by a Hanning (or raised cosine) window function,[36]

$$w(k) = 0.5\left[1 - \cos\left(\frac{2\pi k}{n+1}\right)\right] \qquad (1)$$

which is defined for the point index k in the data segment in terms of the number of data points n. The window function gradually forces the intensity at the beginning and end of the signal segment to zero amplitude. This procedure is required to suppress satellite ripples in the Fourier-magnitude spectra, which result from the leakage of signal frequencies into adjacent channels owing to truncation of the time-domain signal at the beginning and end. Last, the windowed signals were zero-padded by a factor of 32 to enhance the point density along the frequency axis in the Fourier-magnitude spectra.

Figure 7 shows that the oscillatory signals observed in the 808-nm region of the dynamic-absorption spectrum result from rapidly damped low-frequency components and from high-frequency components that persist well past the 4000-fs delay mark. The contour line exhibits a strong low-frequency component that is not as strongly displayed in the transient. The Fourier-magnitude spectra obtained from the contour and transient are shown in Figure 8. The main difference between the two spectra is the strength of the 12-cm^{-1} peak, which is much more intense in the spectrum derived from the contour line. At least eleven components with reproducible position, width, and intensity are observed over the 10−800 cm^{-1} frequency range.

Similar modulation frequencies contribute to the 864-nm region of the dynamic-absorption spectrum. The oscillatory signals obtained from the transient and contour line (see Figure 9) are almost identical; however, again, the Fourier-magnitude spectra shown in Figure 10 indicate a stronger component at 12 cm^{-1} in the contour line. Compared to the strength of the 450-cm^{-1} components, however, the 12-cm^{-1} components detected at 864 nm are substantially weaker than those observed at 808 nm (see Figure 8).

To obtain reliable estimates for intensities and damping times, we modeled the experimental Fourier-magnitude spectra obtained from the contour lines at 808 and 864 nm, using a sum of damped cosines:

$$I(t) = \sum_i A_i \exp\left(-\frac{t}{\gamma_i}\right)\cos(\omega_i t + \phi_i) \qquad (2)$$

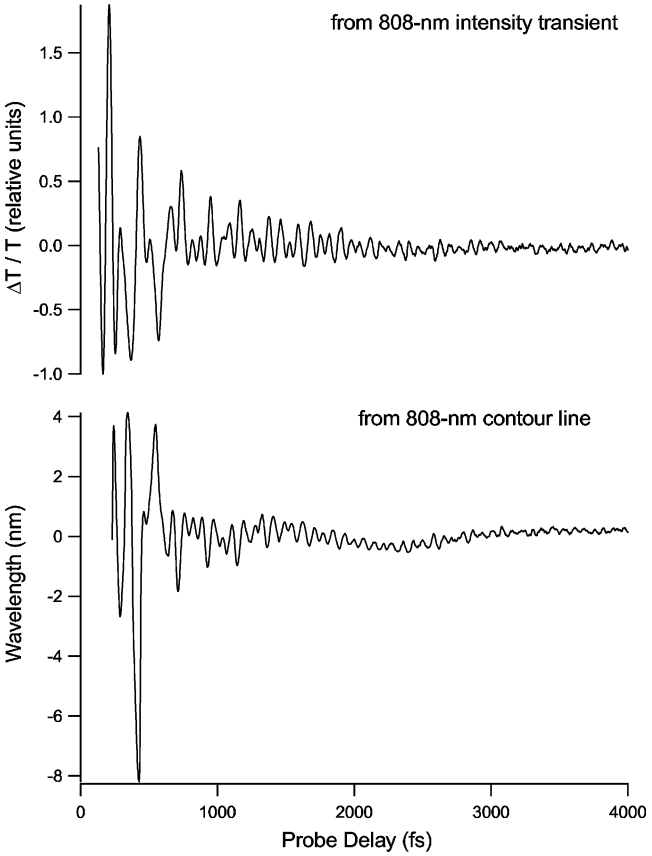

Figure 7. Comparison of the oscillatory components observed at 808 nm from the intensity transient (upper graph) and from the 808-nm contour line (lower graph) obtained from the dynamic-absorption spectrum from IR144 in methanol (see Figure 4).

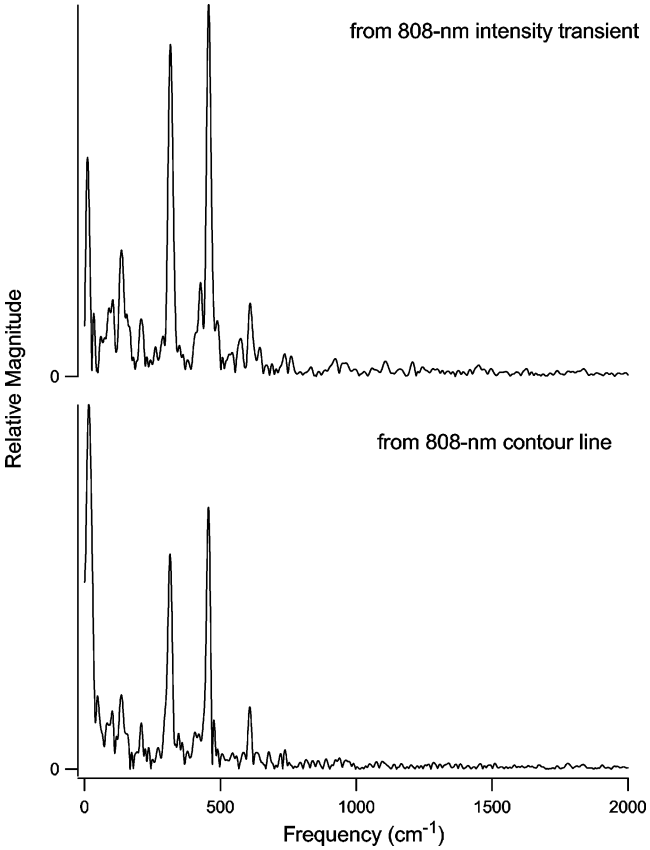

Figure 8. Comparison of the Fourier-magnitude spectra obtained from the oscillatory components observed at 808 nm, as shown in Figure 7, from the intensity transient (upper graph) and from a contour line (lower graph) obtained from the dynamic-absorption spectrum from IR144 in methanol.

The model signal was sampled using the delay times t and segment lengths obtained from the experimental contour signals; it was processed by the same sequence of windowing, zero-padding, and Fourier-magnitude spectrum calculation. The intensities A_i, frequencies ω_i, and damping times γ_i were adjusted iteratively to reproduce the intensity, position, and width of each significant feature in the experimental Fourier-magnitude spectrum. (One might then reliably obtain the phases ϕ_i by optimization *in the time domain*, leaving all other model parameters constant; the phases directly retrieved from a Fourier analysis of the contour lines or transients are strongly affected by signal noise.) The optimized parameters are listed in Table 1. The intensities listed in the table were compensated for the finite width of the instrument-response function by deconvolution in the frequency domain: the raw optimized amplitudes were scaled by the reciprocal of the Fourier magnitude at frequency ω_i obtained from the pump−probe autocorrelation signal.[37] The components listed are those that were reproduced in several experimental trials under the same conditions; the uncertainties reflect the range of observed frequencies. The synthetic spectra shown in Figure 11 were obtained from the tabulated model parameters using a sum of Lorentzian line shapes:[38]

$$I(\omega) = \sum_i \frac{A_i}{4\gamma_i^2(\omega - \omega_i)^2 + 1} \qquad (3)$$

Note that an assumption of Lorentzian line shapes results in a model that damps somewhat more rapidly (especially for the higher-frequency components, such as that at 456 cm^{-1}) than is actually observed.

TABLE 1: Frequencies, Normalized Intensities, and Damping Constants for Modulation Components Observed in Contour Lines at 808 and 864 nm from the Dynamic-Absorption Spectrum of IR144 in Methanol

	808-nm contour		864-nm contour	
frequency (cm^{-1})	intensity[a]	γ (fs)	intensity[a]	γ (fs)
15 ± 6	2.30	600	0.15	800
96 ± 6	0.05	1300	0.03	1300
138 ± 6	0.23	500	0.29	500
273 ± 6	0.26	700	0.10	700
317 ± 2	0.80	750	1.98	500
353 ± 6	0.14	1000	0.07	1000
456 ± 2	1.00	1000	1.00	1000
483 ± 7	0.28	1300		
500 ± 8	0.15	1300		
501 ± 3			0.21	500
525 ± 6			0.12	1300
609 ± 2	0.37	1100	0.68	900
634 ± 2	0.46	500	0.36	1000

[a] Relative to the intensity of the 456-cm^{-1} mode after deconvolution in the frequency domain.

The synthetic spectra shown in Figure 11 represent the best estimates for the modulation frequencies, intensities, and damping times for the coherent wave-packet motions of IR144 that would be retrieved by Fourier analysis if it were possible to determine the spectrum from an infinitely long segment of data obtained from an experiment with delta-function pump pulses. The windowing function causes a significant quenching of signal components below 50 cm^{-1} for the 4000-fs signal length used here; compared to the frequency and peak height obtained directly from the Fourier-magnitude spectrum by inspection, the retrieved frequency is shifted a few wavenumbers higher and

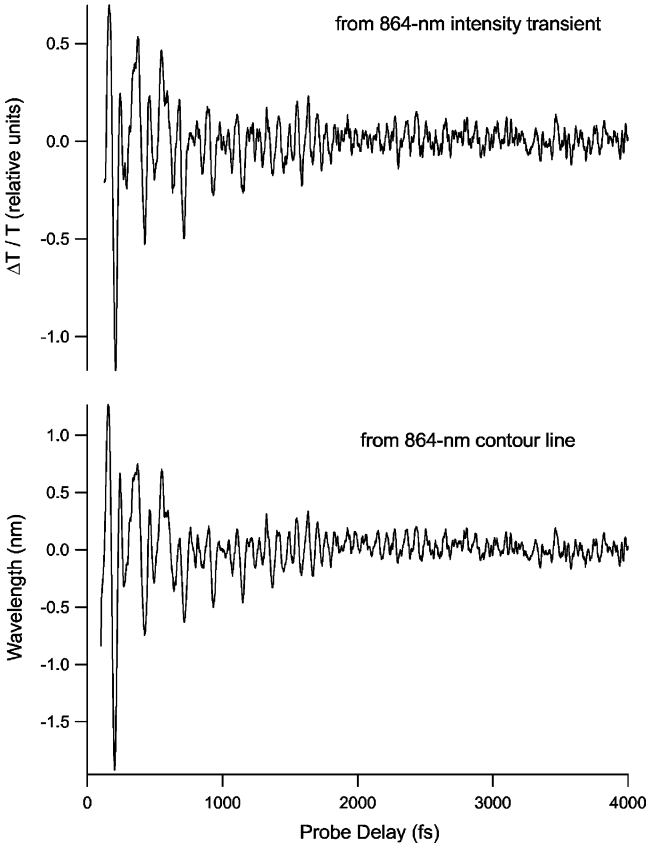

Figure 9. Comparison of the oscillatory components observed at 864 nm from the intensity transient (upper graph) and from the contour line (lower graph) obtained from the dynamic-absorption spectrum from IR144 in methanol.

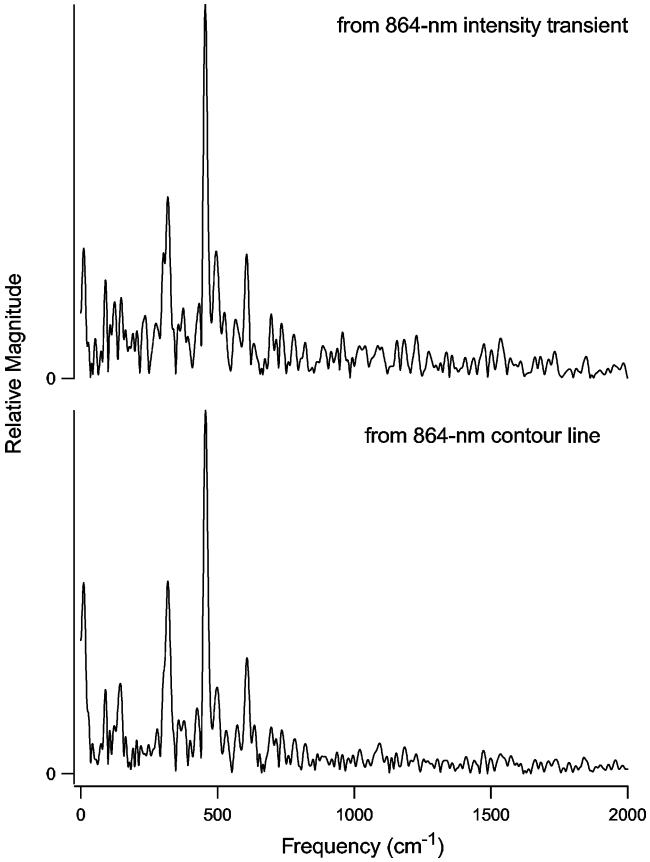

Figure 10. Comparison of the Fourier-magnitude spectra obtained from the oscillatory components observed at 864 nm, as shown in Figure 9, from the intensity transient (upper graph) and from a contour line (lower graph) obtained from the dynamic-absorption spectrum from IR144 in methanol.

the retrieved intensity is significantly larger (for example, compare Figure 11 with Figure 8). Furthermore, the window function causes an inverse scaling of the width of the peaks in the Fourier-magnitude spectrum with respect to the analyzed segment length; longer segments retrieve narrower peaks, but the signal/noise ratio degrades as the delay time increases because of the damping of the oscillations. The frequency-domain spectral-estimation method used here is robust; in the absence of signal/noise limitations, the returned parameters are independent of the choice of analyzed signal length.

Long-Pulse Dynamic-Absorption Experiments. To probe the ground-state depletion portion of the dynamic-absorption spectrum somewhat farther to the blue than was possible in the short-pulse experiments, we performed a set of experiments with pulses of 52-fs ($sech^2$) duration and a spectral width of 11.5 nm from the Mira9000 oscillator, which can be tuned well to the blue of the maximum of the fixed spectrum of our Murnane−Kapteyn oscillator. These experiments also provide a clearer view of the low-frequency wave-packet oscillations because the high-frequency components that dominate the signals obtained with short pulses are not impulsively excited.

Figure 12 shows the dynamic-absorption transient, its oscillatory components, and the Fourier-magnitude spectrum obtained from a pump spectrum centered at 765 nm and transmitted probe light monitored at 758 nm. Three strong components—at 12, 90, and 130 cm^{-1}—are observed in the Fourier-magnitude spectrum; high-frequency modulation components (above 220 cm^{-1}) are not observed reproducibly. The frequencies, intensities, and damping times for the oscillatory components were retrieved using the procedure described in the previous section of the paper. The results are similar to those obtained for the

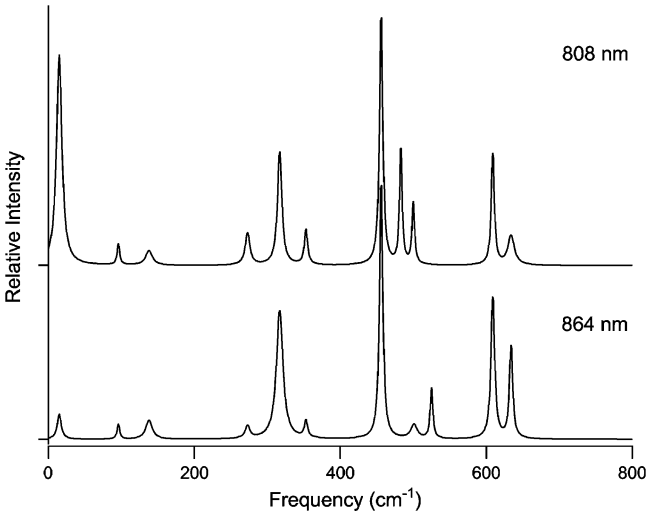

Figure 11. Synthetic spectra describing relative magnitudes, frequencies, and damping times for modulation components observed in the contour lines centered at 808 nm (top graph) and 864 nm (bottom graph) in the dynamic-absorption spectrum of IR144. Lorentzian line shapes were used for each modulation component. Parameters for these spectra are listed in Table 1.

808-nm contour or transient in the short-pulse experiment. Note that the intensity for the 12-cm^{-1} component is more intense than that for the 130-cm^{-1} component, which mirrors the result obtained with 12-fs pulses from the 808-nm contour (see Figure 8 and Table 1) but not that from the 864-nm contour (see Figure 10).

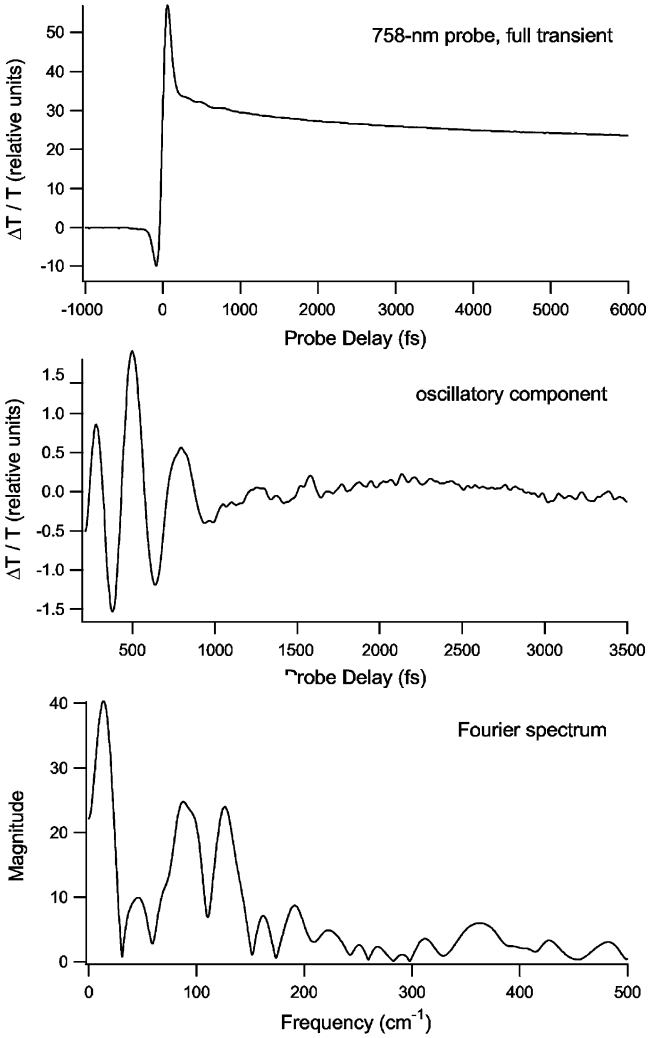

Figure 12. Narrow-spectrum, long-pulse (52-fs) pump−probe transient (top), oscillatory component (middle), and Fourier-magnitude spectrum (bottom) obtained from IR144 in methanol. The pump spectrum and transmitted-probe bandpass were centered at 765 and 758 nm, respectively. Delay window used for the Fourier transform was 3500 fs wide.

An additional experiment was conducted with the pump spectrum centered at 750 nm and the transmitted probe light monitored at 743 nm. These settings probe the ground-state wave-packet motion even farther to the blue but the vibrational level that is prepared on the excited-state surface is higher in energy. The results we obtained (not shown) are very similar to those in Figure 12, but the signal/noise ratio is not as high.

Simulations. The amplitude-modulated portion of the dynamic-absorption spectrum observed from IR144 results from an interference pattern produced by the *partial* spectral overlap of the stimulated-emission and ground-state depletion spectra. In the following, we show how the *phases* of the excited-state and ground-state wave packets that result in the modulated spectra can be discerned by inspection of a contour representation of the dynamic-absorption spectrum. The reader is referred to work by Pollard and Mathies,[12] Sundström and co-workers,[18,39,40] and Nagarajan[41] for a discussion of the nonlinear optics and solvent-bath coupling aspects of the problem. We discuss in the following the use of a simple theory to determine the spectral interference that would be produced by a cosinusoidal motion of two line shapes with respect to the ground-to-excited-state energy gap at one or more vibrational frequencies. The results mimic several aspects of the experimental dynamic-absorption spectra from IR144 that are discussed in this paper.

The stimulated-emission signal I that occurs at a certain time t and observation frequency ω from a single wave packet on the excited-state surface can be described parametrically by a line-shape function, an oscillating equation of motion, and a phase distribution. Here, we use a Gaussian shape of constant intrinsic intensity A and half-width σ:

$$I(\omega,t) = A\sum_i N(\phi_i)\exp\left(-\frac{\omega-\omega_{0i}(t)}{2\sigma^2}\right) \qquad (4)$$

The intensity A scales with the energy of the pump pulse; the width σ can be taken as resulting from homogeneous line broadening and the temperature-dependent breadth of the initial vibrational-state distribution. To obtain a damped modulation of the spectrum, the sum is taken over an ensemble of molecules described by a normalized phase distribution $N(\phi_i)$, defined here as a Gaussian whose width expands exponentially with time; the time constant used arbitrarily in the simulations produces an effective intensity-damping time of 1.2 ps. The center frequency ω_{0i} for the molecules in the ensemble with phase ϕ_i oscillates cosinusoidally with respect to ω as

$$\omega_{0i}(t) = \Delta\cos(\omega_v t + \phi_i) \qquad (5)$$

For a certain vibrational level v, the energy gap for the most probable transition to the other state's potential-energy surface is effectively cosinusoidally modulated as a function of the vibrational coordinate because of the variation in Franck−Condon factors. The amplitude parameter Δ corresponds to the resonance Raman cross section, which is proportional to the square of the dimensionless displacement of the excited-state vibrational coordinate for Albrecht *A*-term active modes. Without some displacement, the spectrum is not modulated, with respect to the vibrational coordinate.[38]

In the first simulation, the mode frequency ω_v was set arbitrarily to 200 cm^{-1}; the amplitude Δ was set to be one-third of the half-width $\sigma = 1$. This choice produces a broad spectrum with a relatively small modulation depth like that of IR144 at room temperature. The intensity surface $I(\omega,t)$ was built as a 400 × 400 grid of intensities that was calculated as a series of time-resolved spectra with a spacing of 5 fs over the 0−2000 fs range.

The contour-plot representation of the stimulated-emission intensity surface shown in Figure 13 can be described as a set of cosinusoidally modulated contour lines that exhibit the same phase. The Fourier-magnitude spectrum of one of the contour lines, as calculated using the methods described previously, consists of a peak at the fundamental frequency and a series of progressively much weaker peaks at the harmonics (see Figure 14, where only the first harmonic at 400 cm^{-1} is barely visible with the fundamental plotted at full scale).

Figure 15 shows that similar Fourier-magnitude spectra with strong fundamentals and much weaker harmonics are obtained from intensity transients obtained as slices across the $I(\omega,t)$ surface at selected observation frequencies ω. Near the center of the spectrum, however, the transients exhibit a much more intense second-harmonic component. Indeed, the wave packet crosses the observation frequency twice per mode period, but the modulation depth at the second-harmonic frequency is not very large except at the center of the spectrum. This behavior has been previously discussed.[16,39,42]

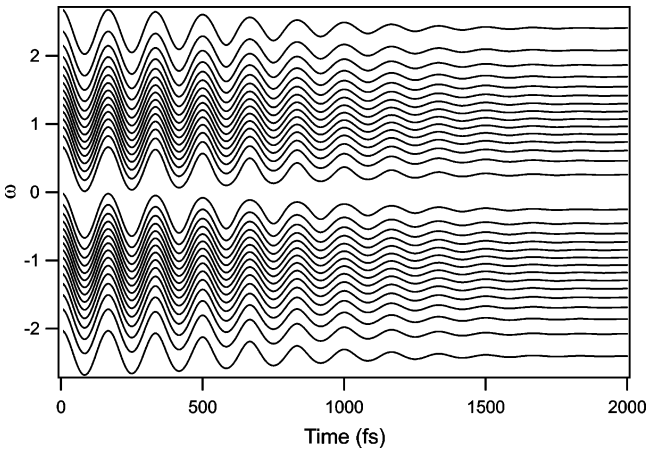

Figure 13. Contour-plot representation of the modulated stimulated-emission spectrum resulting from the 200-cm^{-1} vibrational motion of a single damped wave packet. Parameters for the calculation are described in the text.

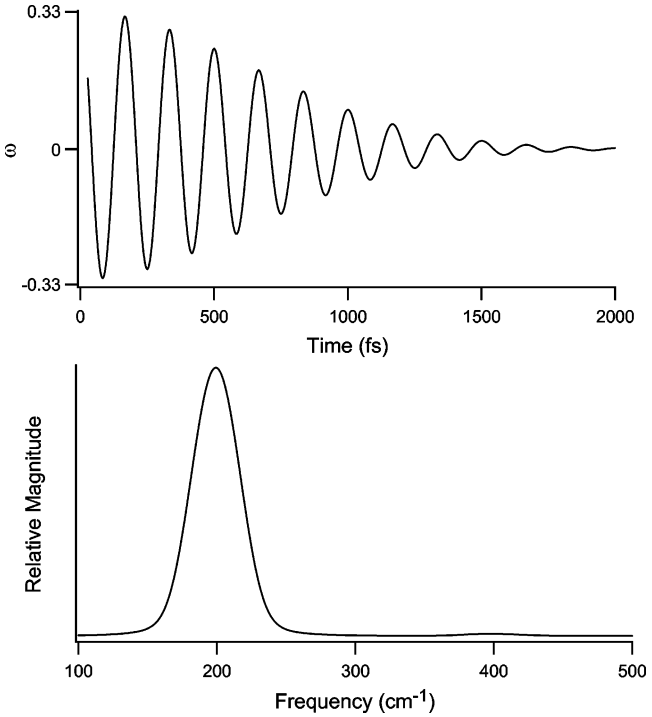

Figure 14. Single contour line selected from the set shown in Figure 13 at $\omega = -1$ and its Fourier-magnitude spectrum (bottom panel).

Figure 15 also shows the intensity-phase behavior of the transients. Recurrences occur at fixed times, independent of ω; near the center of the spectrum, however, the recurrence times scan rapidly from one phase limit to the other and produce a π phase shift. This aspect of the dynamic-absorption spectrum has been discussed in much of the previous work.[9,16,17,19,20] If the narrow spectral region where the phase shift occurs lies outside the probed region or is obscured by a spectral overlap, a plot of the phase as a function of ω might be difficult to interpret.[21] In contrast, the constant contour-phase signature that results from the motion of a single wave packet can be observed over most of the probe region spanned by the spectral motion.

Figure 16 shows the results obtained when a second modulation component is introduced. The calculation was performed as the sum of in-phase components with modulation frequencies at 200 and 120 cm^{-1} and relative intensities of 1 and 0.75, respectively; the other parameters were the same as those in the first simulation. The resulting $I(\omega,t)$ surface exhibits contour lines with two modulation components, as one might expect. It can be shown that the magnitudes obtained from a Fourier analysis of the contour lines are proportional to the product of the amplitude Δ (eq 5) and the intensity-scaling factor A (eq 4). The Fourier-magnitude spectra obtained from single-frequency intensity transients are similar to those obtained from the contour lines.

Last, Figure 17 shows the spectral interference that results from the in-phase motion of two wave packets with the same frequency (200 cm^{-1}) and intensity, but one in the excited-state surface and one in the ground-state surface. In this simulation, we used eq 5, with the parameters specified previously, to control the motion for the stimulated-emission spectrum. The equation of motion for the ground-state depletion spectrum is essentially the negative of that used for the stimulated-emission spectrum:

$$\omega_{0i} = \omega_G - \Delta \cos(\omega_v t + \phi_i) \qquad (6)$$

The ground-state wave packet absorbs probe photons, so the cosinusoidal motion of its signal with respect to ω is opposite in sense to that contributed by the gain of the excited-state wave packet.[43,44] For this simulation, the ground-state and excited-state signals are offset along the ω-axis by the parameter $\omega_G = 1$.

The resulting intensity surface exhibits a set of contour lines with *four* alternating phase regions. As one scans in Figure 17 from the lower ω limit, one encounters a continuous set of contour lines with the same phase that results from the excited-state wave packet. A similar set of lines that result from the ground-state wave packet is observed starting from the upper ω limit; however, the phase is inverted with respect to the phase of the opposite set of contour lines. The observed phase reports which of the two wave-packet signals is the larger one at a particular ω value. However, in the center of the spectrum, the contour phase inverts twice, producing two narrow regions of opposite phase. These regions result from the narrowing of the spectral breadth of the wave packet as it changes its direction of motion; the resulting relatively sharp intensity modulation causes the signal of the turning wave packet to surpass that of the other. Note that these turning-point regions were observed in the spectroscopic simulations by Pollard and Mathies[12,13] even in the limit of purely harmonic motion; they occur in our simulations analogously from the phase distribution $N(\phi_i)$. The turning-point spectral regions that contribute to the phase alternation in the center of the dynamic-absorption spectrum result from the *short-displacement* and *long-displacement* turning points of the excited-state and ground-state wave-packet motion, respectively. The other two turning-point spectral regions would be found in the clear (not overlapped with the signal from the other wave packet) high-frequency and low-frequency limits of the spectrum. Figure 18 illustrates the positions on the vibrational-displacement axis where the turning points can be found.

The pattern of phase alternation shown in Figure 17 is very similar to that observed in the spectrum from IR144 (see Figure 4); the main differences involve a rapid relaxation of the energy of the excited state that is due to dynamic solvation, which is not included in the simulation. The reader should refer to the work by Nagarajan[41] for a treatment of this issue.

4. Discussion

The results of this paper show that a contour representation of the dynamic-absorption spectrum provides a powerful and

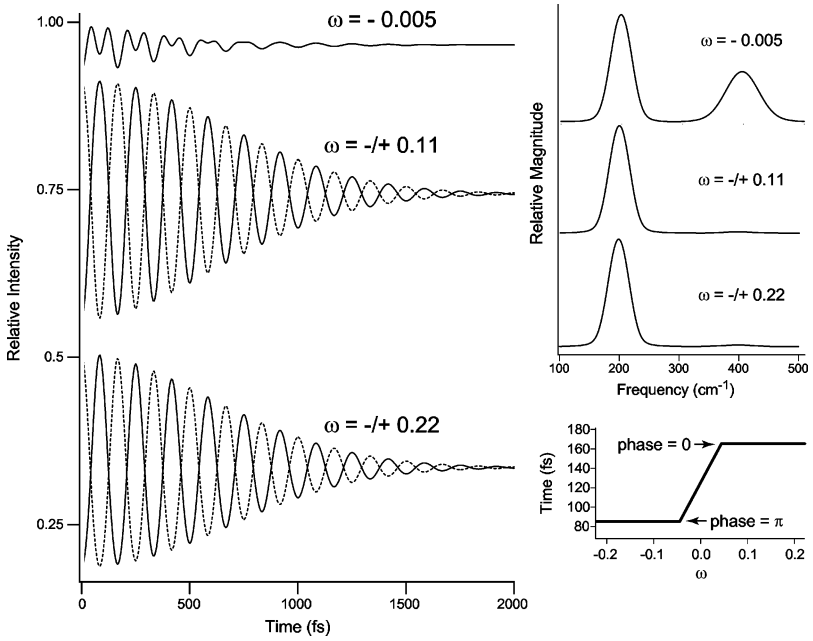

Figure 15. Transients obtained from the spectrum shown in Figure 13 at a set of discrete observation frequencies ω. Where pairs of transients are superimposed, solid curves correspond to $\omega < 0$ and dashed curves correspond to $\omega > 0$. Fourier-magnitude spectra corresponding to the transients are shown to the right, and the lower right-hand figure plots the first positive-going recurrence time as a function of ω.

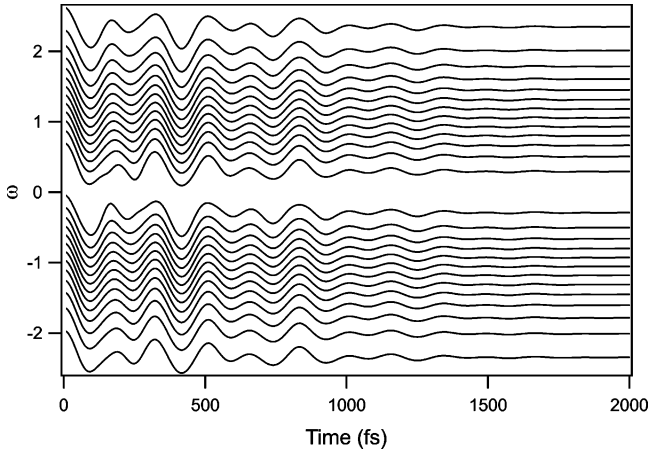

Figure 16. Contour-plot representation of the modulated stimulated-emission spectrum resulting from the motion of a damped wave packet with two modulation components, at 200 and 120 cm^{-1} and with relative intensities of 1 and 0.75, respectively. Parameters for the calculation are otherwise as used for the simulation shown in Figure 13.

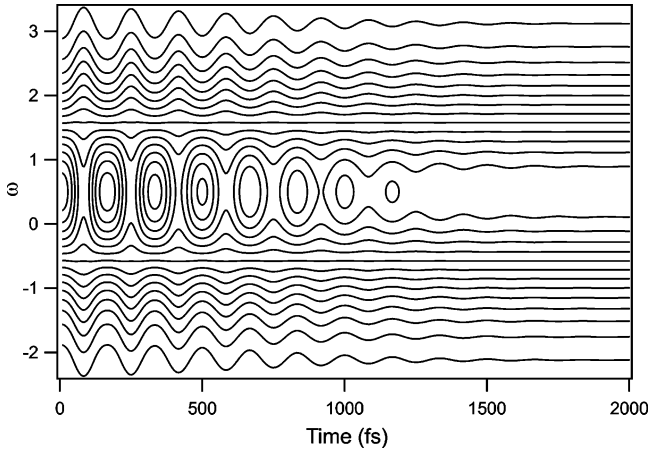

Figure 17. Contour-plot representation of the sum of the modulated stimulated-emission and ground-state depletion spectra resulting from two damped wave packets: one moving on the excited-state surface and one moving on the ground-state surface. Both spectra are modulated by the same 200-cm^{-1} component but they move with opposite sense, with respect to the observation-frequency axis, ω. Parameters for the stimulated-emission spectrum are as used for the spectrum shown in Figure 13; the antisense (ground-state) spectrum is offset along the ω-axis from the first wave packet by +1 unit.

easily used tool that permits a distinction on the basis of the vibrational phase between coherent wave-packet motions on a molecule's ground-state and excited-state potential-energy surfaces, even in the limit of small Stokes shifts. The experimental results from IR144 and the simulations show that a Fourier analysis of contour lines returns essentially the same modulation frequencies and relative magnitudes that a Fourier analysis of intensity transients provides. There may be a technical advantage in the analysis of the contour lines because of their direct sensitivity to modulation with respect to the probe wavelength, the main signature of coherent wave-packet motion. Furthermore, the experimental results suggest that contour lines are more sensitive to very low frequency modulations, which are inherently difficult to detect against a background of noise. However, the main value of the contour representation lies in its direct projection of the phase relationships between pump−probe signals observed at different observation frequencies.

The antiphase character of the contour waveforms produced by the excited-state and ground-state wave packets in dynamic-absorption spectra results naturally from stimulated emission and absorption, respectively, when the wave packets are resonant with probe photons.[10−13] As depicted in Figure 18, the pump field prepares an excited-state wave packet at the Franck−Condon geometry. The excited-state wave packet generally is prepared on a sloping, displaced region of the excited-state surface because of the change in electronic configuration that accompanies absorption of the pump photon. The ground-state wave packet is created by an interaction of the now-moving excited-state wave packet with the pump field. The momentum of the parent excited-state wave packet is conserved in this process; therefore, the excited-state and ground-state wave packets move in phase away from the Franck−Condon geometry. Because the excited-state surface is displaced, however, the recurrence time for the excited-state wave packet is

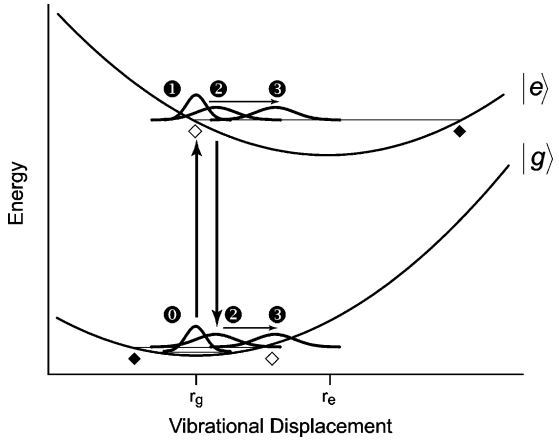

Figure 18. Excited-state and ground-state coherent wave-packet motion in the dynamic-absorption experiment. The excited-state ($|e\rangle$) and ground-state ($|g\rangle$) potential-energy surfaces are drawn as parabolas that are displaced with respect to a generalized multimode coordinate; r_g and r_e mark the equilibrium ground-state and excited-state geometries, respectively. Thick arrows represent the resonant pump-laser field; thin arrows show the direction that the wave packets evolve during the first passage on the two surfaces. The numbers indicate event times, starting with the ground-state probability density ($t = 0$), creation of the excited-state wave packet by the pump field ($t = 1$), creation of the ground-state wave packet by the pump field ($t = 2$), and evolution during the first vibration ($t = 3$). The *turning-point* regions, where a wave packet narrows and reverses its direction of motion, are marked on both surfaces with diamonds; white (unfilled) diamonds mark the turning points that contribute to the interference pattern in the dynamic-absorption spectrum.

somewhat delayed (for positive excited-state displacements) with respect to that of the ground-state wave packet.[12] In the limit of zero displacement and bound surfaces, the contour waveforms exhibited by the excited-state and ground-state wave packets would be exactly antiphase in character if the same modes are active on both surfaces. Both wave packets would describe the same equation of motion (structure as a function of time), but they act *oppositely* on the transmitted probe intensity. Any phase shift between the resulting antiphase waveforms reports the displacement directly, and mode-specific displacements might be obtained from an analysis of the phases for individual modes, as preferably obtained by optimization of a model in the time domain.

Ground-State and Excited-State Wave-Packet Motion in IR144. The four regions of alternating phase that are observed in the contour representation of the dynamic-absorption spectrum of IR144 (see Figure 4) define the spectral regions in which excited-state and ground-state wave-packet modulations can be observed. We chose to characterize in detail the 808- and 864-nm regions (see Figures 5−10) because they lie in regions where the ground-state and excited-state wave packets, respectively, make a dominant contribution. The 808-nm region lies in the lower energy of the two turning-point regions of the spectrum, so we can use contour lines and intensity transients in this portion of the spectrum to obtain information on ground-state wave-packet motions. The 864-nm region lies in the long-wavelength-limit continuous run of contour lines that result from the motions of the excited-state wave packet.

The contour waveforms observed at 808 nm in the ground-state turning-point region and at 864 nm in the excited-state region (see Figure 6) are almost exactly antiphase at early delays. This finding indicates that the low-frequency normal coordinates of IR144 have only small displacements. The increasing phase difference between the two waveforms that is observed with increasing delay reports small differences in the excited-state and ground-state vibrational frequencies; however, Table 1 indicates that only two weak components out of eleven modes exhibit significant frequency shifts (and, surprisingly, the excited state exhibits higher frequencies in these two modes). Given the lack of large frequency shifts and displacements along the low-frequency coordinates, these modes probably gain some of their activity through anharmonic coupling to high-frequency modes that are not impulsively excited in these experiments. These high-frequency modes are likely to be those of totally symmetric character that obtain resonance Raman intensity[45] from the Albrecht *A*-term mechanism; the low-frequency modes also may obtain their intensities via the *B*-term mechanism because of mixing of the Franck−Condon state with other electronic states in the energy neighborhood.

The 15-cm^{-1} feature, which is observed much more prominently in the ground-state wave-packet motion, is the most interesting in this regard. The relatively strong ground-state intensity shows that the excited-state wave packet is moving near the Franck−Condon region with some significant amplitude along the normal coordinate(s) associated with this feature.[14] The much weaker excited-state intensity suggests that the wave packet moves rather quickly, well within the period of the vibration of this coordinate, to a region of the excited-state potential-energy surface that is relatively flat with respect to the low-frequency coordinate(s). This motion is associated with several vibrations along the higher-frequency coordinates.

Nature of the Lowest-Frequency Vibrations of IR144. Lacking a systematic isotopic-substitution study, it is not possible at this point to provide definitive assignments for the low-frequency modes that are active in the vibrational coherence on the ground and excited states of IR144. Nevertheless, through the use of ground-state electronic structure calculations and normal-mode calculations from the optimized geometries, we can suggest probable assignments in terms of classes of motion, with respect to the conjugated-polyene backbone of IR144.

We used Gaussian98[46] to perform a series of calculations at various levels of theory. The structures that were electronically and structurally peripheral in IR144 to the conjugated polyene—the piperazinyl ring and the propylsulfonyl tails—were truncated to dimethylamine and methyl groups, respectively. These simplifications are reasonable because the resonant electronic transition in the dynamic-absorption experiments is a $\pi \rightarrow \pi^*$ transition. The UFF molecular-mechanics force field was used to obtain an approximate structure; the optimized structure was then used, in series, to obtain optimized structures in the ground state with the AM1 semiempirical theory and then the B3LYP hybrid density-functional theory with the 6-31G(d) basis set. Good minima were located on the ground-state surface in each case. From each optimized structure, the normal modes and frequencies were obtained with the same theory used to optimize the geometry.

The most significant result of the AM1 and B3LYP calculations is that IR144 should exhibit three *global* normal modes with estimated frequencies in the 10−15 cm^{-1} regime. These modes should exhibit resonance Raman intensity because they involve distortions of the conjugated polyene. The mode with the lowest frequency in this range can be described as a hindered torsion; the central five-membered ring (see Figure 1) resists large displacements along this coordinate, which, in the ring's absence, would contribute to isomerization of the central C=C bond. The other two modes, which result from in-plane and out-of-plane deformations, are almost degenerate. We suggest that the prominent 15-cm^{-1} feature, observed especially in the ground-state vibrational coherence, can be assigned to the

superimposed line shapes that result from the three global modes. The intensity difference noted for ground-state and excited-state vibrational coherence in the 15-cm^{-1} mode might be interpreted, then, as an indication that a significant distortion of the conjugated polyene along at least one of the global coordinates occurs within one vibrational period. This geometry change will contribute to the intramolecular (nonsolvation) portion of the decay of the ground-excited-state energy-gap time-correlation function $M(t)$, which has been detected in stimulated photon-echo and dynamic fluorescence Stokes shift experiments.[24−26]

Acknowledgment. This research was supported by a grant from the Molecular Biophysics program of the National Science Foundation. Additional support for instrumentation was obtained from the Michigan Structural Biology Center at Michigan State University, which is funded by the Michigan Life Sciences Corridor Program.

References and Notes

(1) Brito Cruz, C. H.; Fork, R. L.; Knox, W. H.; Shank, C. V. *Chem. Phys. Lett.* **1986**, *132*, 341−345.

(2) Brito Cruz, C. H.; Gordon, J. P.; Becker, P. C.; Fork, R. L.; Shank, C. V. *IEEE J. Quantum Elect.* **1988**, *24*, 261−266.

(3) Mathies, R. A.; Brito Cruz, C. H.; Pollard, W. T.; Shank, C. V. *Science* **1988**, *240*, 777−779.

(4) Pollard, W. T.; Brito Cruz, C. H.; Shank, C. V.; Mathies, R. A. *J. Chem. Phys.* **1989**, *90*, 199−208.

(5) Fragnito, H. L.; Bigot, J.-Y.; Becker, P. C.; Shank, C. V. *Chem. Phys. Lett.* **1989**, *160*, 101−104.

(6) Schoenlein, R. W.; Peteanu, L. A.; Mathies, R. A.; Shank, C. V. *Science* **1991**, *254*, 412−415.

(7) Dexheimer, S. L.; Wang, Q.; Peteanu, L. A.; Pollard, W. T.; Mathies, R. A.; Shank, C. V. *Chem. Phys. Lett.* **1992**, *188*, 61−66.

(8) Peteanu, L. A.; Schoenlein, R. W.; Wang, Q.; Mathies, R. A.; Shank, C. V. *Proc. Natl. Acad. Sci. U.S.A.* **1993**, *90*, 11762−11766.

(9) Wang, Q.; Schoenlein, R. W.; Peteanu, L. A.; Mathies, R. A.; Shank, C. V. *Science* **1994**, *266*, 422−424.

(10) Pollard, W. T.; Fragnito, H. L.; Bigot, J.-Y.; Shank, C. V.; Mathies, R. A. *Chem. Phys. Lett.* **1990**, *168*, 239−245.

(11) Pollard, W. T.; Lee, S.-Y.; Mathies, R. A. *J. Chem. Phys.* **1990**, *92*, 4012−4029.

(12) Pollard, W. T.; Mathies, R. A. *Annu. Rev. Phys. Chem.* **1992**, *43*, 497−523.

(13) Pollard, W. T.; Dexheimer, S. L.; Wang, Q.; Peteanu, L. A.; Shank, C. V.; Mathies, R. A. *J. Phys. Chem.* **1992**, *96*, 6147−6158.

(14) Myers, A. B.; Mathies, R. A. In *Resonance Raman Spectra of Polyenes and Aromatics*; Spiro, T. G., Ed.; Biological Applications of Raman Spectroscopy, Vol. 2; Wiley−Interscience: New York, 1987; pp 1−58.

(15) Bowman, R. M.; Dantus, M.; Zewail, A. H. *Chem. Phys. Lett.* **1990**, *174*, 546−552.

(16) Vos, M. H.; Rappaport, F.; Lambry, J.-C.; Breton, J.; Martin, J.-L. *Nature* **1993**, *363*, 320−325.

(17) Zhu, L.; Sage, J. T.; Champion, P. M. *Science* **1994**, *266*, 629−632.

(18) Chachisvilis, M.; Fidder, H.; Pullerits, T.; Sundström, V. *J. Raman Spectrosc.* **1995**, *26*, 513−522.

(19) Bardeen, C. J.; Wang, Q.; Shank, C. V. *J. Phys. Chem. A* **1998**, *102*, 2759−2766.

(20) Rosca, F.; Kumar, A. T. N.; Ye, X.; Sjodin, T.; Demidov, A.; Champion, P. M. *J. Phys. Chem. A* **2000**, *104*, 4280−4290.

(21) Diffey, W. M., Ph.D. Thesis, Vanderbilt University, Nashville, TN, 2002.

(22) Pshenichnikov, M. S.; Duppen, K.; Wiersma, D. A. *Phys. Rev. Lett.* **1995**, *74*, 674−677.

(23) de Boeij, W. P.; Pshenichnikov, M. S.; Wiersma, D. A. *J. Phys. Chem.* **1996**, *100*, 11806−11823.

(24) Joo, T.; Jia, Y.; Yu, J.-Y.; Lang, M. J.; Fleming, G. R. *J. Chem. Phys.* **1996**, *104*, 6089−6108.

(25) Passino, S. A.; Nagasawa, Y.; Joo, T.; Fleming, G. R. *J. Phys. Chem. A* **1997**, *101*, 725−731.

(26) Nagasawa, Y.; Passino, S. A.; Joo, T.; Fleming, G. R. *J. Chem. Phys.* **1997**, *106*, 4840−4852.

(27) Shang, X.; Benderskii, A. V.; Eisenthal, K. B. *J. Phys. Chem. B* **2001**, *105*, 11578−11585.

(28) Lakowicz, J. R. *Principles of Fluorescence Spectroscopy*, 2nd ed.; Kluwer Academic/Plenum Publishers: New York, 1999.

(29) Diffey, W. M.; Beck, W. F. *Rev. Sci. Instrum.* **1997**, *68*, 3296−3300.

(30) Diffey, W. M.; Homoelle, B. J.; Edington, M. D.; Beck, W. F. *J. Phys. Chem. B* **1998**, *102*, 2776−2786.

(31) Huang, C.-P.; Asaki, M. T.; Backus, S.; Murnane, M. M.; Kapteyn, H. C. *Opt. Lett.* **1992**, *17*, 1289−1291.

(32) Asaki, M. T.; Huang, C.-P.; Garvey, D.; Zhou, J.; Kapteyn, H. C.; Murnane, M. M. *Opt. Lett.* **1993**, *18*, 977−979.

(33) Edelstein, D. C.; Romney, R. B.; Scheuermann, M. *Rev. Sci. Instrum.* **1991**, *62*, 579−583.

(34) Alavi, D. S.; Hartman, R. S.; Waldeck, D. H. *J. Chem. Phys.* **1990**, *92*, 4055−4066.

(35) Cantor, C. R.; Schimmel, P. R. *Biophysical Chemistry. Part II: Techniques for the Study of Biological Structure and Function*; W. H. Freeman and Company: San Francisco, CA, 1980.

(36) Press, W. H.; Flannery, B. P.; Teukolsky, S. A.; Vetterline, W. T. *Numerical Recipes: The Art of Scientific Computing*; Cambridge University Press: Cambridge, 1986.

(37) McMorrow, D.; Lotshaw, W. T. *Chem. Phys. Lett.* **1990**, *174*, 8594.

(38) McHale, J. L. *Molecular Spectroscopy*; Prentice Hall: Upper Saddle River, NJ, 1999.

(39) Chachisvilis, M.; Pullerits, T.; Jones, M. R.; Hunter, C. N.; Sundström, V. *Chem. Phys. Lett.* **1994**, *224*, 345−351.

(40) Chachisvilis, M.; Sundström, V. *Chem. Phys. Lett.* **1996**, *261*, 165−174.

(41) Nagarajan, V. *Chem. Phys. Lett.* **2000**, *317*, 203−210.

(42) Jonas, D. M.; Bradforth, S. E.; Passino, S. A.; Fleming, G. R. *J. Phys. Chem.* **1995**, *99*, 2594−2608.

(43) Scherer, N. F.; Ziegler, L. D.; Fleming, G. R. *J. Chem. Phys.* **1992**, *96*, 5544−5547.

(44) Scherer, N. F.; Jonas, D. M.; Fleming, G. R. *J. Chem. Phys.* **1993**, *99*, 153−168.

(45) Tang, J.; Albrecht, A. C. In *Raman Spectroscopy: Theory and Practice*; Szymanski, H. A., Ed.; Plenum: New York, 1970; Vol. 2, pp 33−68.

(46) Frisch, M. J.; Trucks, G. W.; Schlegel, H. B.; Scuseria, G. E.; Robb, M. A.; Cheeseman, J. R.; Zakrzewski, V. G.; J. A. Montgomery, J.; Stratmann, R. E.; Burant, J. C.; Dapprich, S.; Millam, J. M.; Daniels, A. D.; Kudin, K. N.; Strain, M. C.; Farkas, O.; Tomasi, J.; Barone, V.; Cossi, M.; Cammi, R.; Mennucci, B.; Pomelli, C.; Adamo, C.; Clifford, S.; Ochterski, J.; Petersson, G. A.; Ayala, P. Y.; Cui, Q.; Morokuma, K.; Salvador, P.; Dannenberg, J. J.; Malick, D. K.; Rabuck, A. D.; Raghavachari, K.; Foresman, J. B.; Cioslowski, J.; Ortiz, J. V.; Baboul, A. G.; Stefanov, B. B.; Liu, G.; Liashenko, A.; Piskorz, P.; Komaromi, I.; Gomperts, R.; Martin, R. L.; Fox, D. J.; Keith, T.; Al-Laham, M. A.; Peng, C. Y.; Nanayakkara, A.; Challacombe, M.; Gill, P. M. W.; Johnson, B.; Chen, W.; Wong, M. W.; Andres, J. L.; Gonzalez, C.; Head-Gordon, M.; Replogle, E. S.; Pople, J. A. *Gaussian 98*, revision A.11.1; Gaussian, Inc.: Pittsburgh, PA, 2001.